Medical Image Analysis 15 (2011) 112–124

Contents lists available at ScienceDirect

Medical Image Analysis

journal homepage: www.elsevier.com/locate/media

A strain energy filter for 3D vessel enhancement with application to pulmonary CT images

Changyan Xiao [a,c,*], Marius Staring [a], Denis Shamonin [a], Johan H.C. Reiber [a], Jan Stolk [b], Berend C. Stoel [a]

[a] Division of Image Processing, Department of Radiology, Leiden University Medical Center, P.O. Box 9600, 2300 RC, Leiden, The Netherlands
[b] Department of Pulmonology, Leiden University Medical Center, P.O. Box 9600, 2300 RC, Leiden, The Netherlands
[c] College of Electrical and Information Engineering, Hunan University, 410082 Changsha, PR China

ARTICLE INFO

Article history:
Received 19 September 2009
Received in revised form 28 July 2010
Accepted 24 August 2010
Available online 24 September 2010

Keywords:
Vessel enhancement
Strain energy density
Shape discrimination
Pulmonary image analysis

ABSTRACT

The traditional Hessian-related vessel filters often suffer from detecting complex structures like bifurcations due to an over-simplified cylindrical model. To solve this problem, we present a shape-tuned strain energy density function to measure vessel likelihood in 3D medical images. This method is initially inspired by established stress–strain principles in mechanics. By considering the Hessian matrix as a stress tensor, the three invariants from orthogonal tensor decomposition are used independently or combined to formulate distinctive functions for vascular shape discrimination, brightness contrast and structure strength measuring. Moreover, a mathematical description of Hessian eigenvalues for general vessel shapes is obtained, based on an intensity continuity assumption, and a relative Hessian strength term is presented to ensure the dominance of second-order derivatives as well as suppress undesired step-edges. Finally, we adopt the multi-scale scheme to find an optimal solution through scale space. The proposed method is validated in experiments with a digital phantom and non-contrast-enhanced pulmonary CT data. It is shown that our model performed more effectively in enhancing vessel bifurcations and preserving details, compared to three existing filters.

1. Introduction

Pulmonary vessel detection plays an important role in computer analysis of lung CT images. Evaluating the vessel is of considerable value to diagnosing for example pulmonary emboli and determining over-distention as an index of pulmonary hypertension. Additionally, there is a great interest in identifying the vascular trees as a set of landmarks, which would allow for matching lungs across volume changes and over time (Hoffman et al., 2003). Based on the anatomical fact that vascular trees usually do not cross well-developed lobar boundaries, the vessel segmentation can also be used to infer lobar location in the absence of fissures (Kuhnigk et al., 2003; Sluimer et al., 2006; Ukil and Reinhardt, 2009). However, accurate and robust detection of pulmonary vessels still remains a problem because of the geometrical complexity and fine characteristics of detailed vascular structures. Especially, with non-contrast-enhanced images being widely used in CT densitometry (Adams et al., 1991; Stoel and Stolk, 2004; Hoffman et al., 2006), the vascular detection becomes even more challenging.

2. Related work

There has been a long history for usage of image intensity derivatives in estimating object shape. Haralick et al. (1983) originally proposed a scheme to describe the topographic primal sketch or structure (e.g. ridge, valley, peak, plane, saddle and hillside) with the first- and second-order directional derivatives.

Blood vessels in medical images can be referred as linear or tubular structures since it can be locally approximated as a line along the branch. The utilization of the second-order Hessian matrix in vessel detection is ascribed to several seminal works (Koller et al., 1995; Sato et al., 1997, 1998; Lorenz et al., 1997; Frangi et al., 1998). From the Taylor expansion, the local intensity variation can be expressed in terms of intensity derivatives. Usually, only the first- and second-order derivatives, i.e. gradient and Hessian matrix are considered. When the gradient is negligible, the Hessian matrix is able to act as an indicator of local structures. As an idealized model, it is assumed that the image intensity in a vessel is constant along the axial direction and takes a Gaussian-shaped profile perpendicular to the central axis (see Krissian et al. (2000) for accurate modeling). With this assumption, the Hessian matrix

* Corresponding author at: College of Electrical and Information Engineering, Hunan University, 410082 Changsha, PR China. Tel.: +86 731 88828348; fax: +86 731 88822606.
E-mail addresses: xcy19722@hotmail.com (C. Xiao), M.Staring@lumc.nl (M. Staring), D.P.Shamonin@lumc.nl (D. Shamonin), J.H.C.Reiber@lumc.nl (J.H.C. Reiber), J.Stolk.long@lumc.nl (J. Stolk), B.C.Stoel@lumc.nl (B.C. Stoel).

1361-8415/$ - see front matter © 2010 Elsevier B.V. All rights reserved.
doi:10.1016/j.media.2010.08.003

would have one eigenvalue close to zero, and the remaining two would have high magnitude with signs determined by object contrast. An elliptical representation was proposed by Frangi et al. (1998), which gave an intuitively geometrical description about the second derivative model. The application of Hessian-based filters varies from tissue visualization (Sato et al., 2000), vasculature segmentation (Descoteaux et al., 2008), to stenosis quantification (van Bemmel et al., 2004). In spite of the encouraging results in vessel branch enhancement, the traditional multi-scale Hessian filters are limited in handling local deformations like vascular junctions due to their essentially single cylinder assumption.

Many vessel extraction methods, e.g. matched filter (Sofka and Stewart, 2006), model-based detection (Mahadevan et al., 2004), suffer from the common problem of an over-simplified tube model. Several efforts have been made to relax this strong shape constraint to accommodate more general vascular structures. The "shape prior" techniques (Nain et al., 2004; Manniesing et al., 2007; Gooya et al., 2008) used certain prediction mechanism to obtain the anisotropic information from previous iterations, which forms a new speed term to guide current front evolution, under the level-set framework. The vessel enhancing diffusion method (Manniesing et al., 2006) integrated a smooth vesselness measure with a non-linear anisotropic diffusion scheme. With diffusion strength and orientation tuned by the local vessel likelihood, this model can enhance vessel structures and tend to preserve intensity homogeneity across non- and weak-vessel regions. A first-order derivative correlation-based filter was proposed by Agam et al. (2005) for vessel enhancement in thoracic CT scans. They adopted an iterative selection scheme to find more than one principal component directions, which are formulated explicitly to discriminate vessel branches, bifurcations and nodules within an adaptive neighborhood. In addition, the directional filter bank was also combined with the Hessian-based filter (Truc et al., 2009). Based on directional image decomposition, this method helps to avoid vessel junction suppression and reveals more thin and continuous vessel structures. Recently, Qian et al. (2009) presented a non-parametric vessel detection method. It is motivated by the observation that the change of intensities in at least one conical-shaped neighborhood region (whose tip is at the voxel of interest) is very small if this conical region lies inside a blood vessel, and high otherwise. This assumption of intensity continuity made the technique adaptable to most vessel structures including ordinary vessel branch, bifurcation and end points.

In this paper, we will present a 3D vessel enhancing model with a main purpose to break the cylinder limits of traditional Hessian filters and improve their ability in preserving more general vascular structures like bifurcations. The method is initially motivated by a recent achievement of stress and strain theory in solid mechanics (Criscione et al., 2000), which has been introduced previously to fMRI imaging by Ennis and Kindlmann (2006). We establish the idea basically on a link between image structures and local loading states of material, due to the mathematical equivalence between image Hessian matrix and mechanical stress tensor. Our main work comprises introducing strain energy density as a measure of structure strength, investigating the Hessian eigenvalue distribution of general vascular shapes, and defining a flexible shape discrimination function from orthogonal tensor decomposition. This model is called a strain energy filter since its response is a weighted strain energy density tuned to specific vessel shapes. As we also use the Hessian eigenvalues to formulate shape discrimination, the strain energy model can be considered a direct generalization of vesselness filters (Frangi et al., 1998).

The remaining paper is organized as follows. We first retrospect the stress tensor decomposition and physical meaning of corresponding invariants in Section 3. Section 4 elaborates on the development of our method. Section 5 gives the experimental results on digital phantom and clinical datasets. In Section 6, the conclusions are discussed.

3. Theoretical background

The Hessian matrix H_σ of a 3D image I at scale σ is equivalent to a stress tensor in solid mechanics (Bower, 2009) in that it is a second-order symmetrical real tensor with $H_\sigma^{ij} = \partial^2 I_\sigma / \partial x_i \partial x_j$. In the following, the subscript σ of H_σ will be omitted for brevity. Like stress tensors, H can be decomposed into an eigensystem of three real eigenvalues λ_i and three mutually orthogonal eigenvectors $\vec{e}_i (i = 1, 2, 3)$.

In tensor analysis, the inner product operator is termed contraction, which is denoted by a colon (:). The contraction of two tensors U and V is defined as

$$U : V = tr(UV^t), \tag{1}$$

where $tr()$ is the trace operator, and t the transposition. If $U{:}V = 0$, the two tensors are orthogonal. Similarly, the tensor magnitude can also be defined using tensorial contraction and is equivalent to the Frobenius norm: $\|U\|_F = \sqrt{U : U}$.

A common decomposition of the stress tensor H is expressed as

$$H = \overline{H} + \widetilde{H}, \tag{2}$$

where $\overline{H}$ corresponds to the so-called "isotropic" or spherical component since it represents the mean stress and is homogeneous in varying orientations. $\widetilde{H}$ indicates the "deviatoric" or anisotropic component, and contains the directional inequality information of stress. They are calculated as follows:

$$\overline{H} = \frac{1}{3} tr(H)\mathbf{1} = \frac{1}{3}(H : \mathbf{1})\mathbf{1}, \tag{3}$$

$$\widetilde{H} = H - \frac{1}{3} tr(H)\mathbf{1} = H - \frac{1}{3}(H : \mathbf{1})\mathbf{1}. \tag{4}$$

Here, $\mathbf{1}$ is the identity matrix. According to the stress principle (Bower, 2009), only the isotropic component causes volume changes, while the deviatoric component exclusively accounts for the distortion or shear without volume changes. Since $\overline{H} : \widetilde{H} = 0$, Eq. (2) is an orthogonal decomposition of H. From this, Criscione et al. (2000) introduced a set of orthogonal tensor invariants K_i for the analysis of hyperelastic strain energy:

$$K_1 = tr(H), \tag{5}$$

$$K_2 = \|\widetilde{H}\|_F, \tag{6}$$

$$K_3 = 3\sqrt{6}\det(\widetilde{H}/\|\widetilde{H}\|_F), \tag{7}$$

where det() is the determinant operator. These invariants are natural descriptions of local deformation in a loaded solid. Here, we use the term "loaded" to represent the state in which forces are being exerted. Due to orthogonal decomposition, the three invariants reflect mutually independent properties of the deformation. The intuitive physical meaning behind them is that K_1 represents the amount of dilatation (with a negative value corresponding to compression), K_2 the magnitude of distortion, and K_3 the mode or type of distortion. For easy understanding, the above three equations can be rewritten in terms of the eigenvalues λ_i of H as well as their first three central moments μ_1 (mean), μ_2(variance) and μ_3:

$$K_1 = \lambda_1 + \lambda_2 + \lambda_3 = 3\mu_1, \tag{8}$$

$$K_2 = \sqrt{\sum_{i=1}^{3}(\lambda_i - \mu_1)^2} = \sqrt{3\mu_2} \tag{9}$$

$$K_3 = \lambda_1\lambda_2\lambda_3 / \|\widetilde{H}\|_F^3 = \sqrt{2}\mu_3\mu_2^{-3/2}. \tag{10}$$

Note that K_3 is actually the skewness of eigenvalues. Ennis and Kindlmann (2006) named these invariants the "cylindrical invariant

set", and used it for analysis and visualization of diffusion tensors in fMRI images. However, the diffusion tensor is different from Hessian matrix: it must be positive-definite, i.e. all eigenvalues are larger than zero. The Hessian matrix has real eigenvalues, which may be positive or negative.

4. Method

The development of our vessel filter is divided into six parts. In Section 4.1, we define the invariant K_1 as a measure of brightness contrast. A strain energy density function is introduced to measure the image structure strength in Section 4.2. Based on the intensity continuity assumption, a description of the Hessian eigenvalue distribution for general vascular structures is obtained in Section 4.3. To ensure the dominance of second-order derivatives, Section 4.4 presents a relative Hessian strength to suppress undesired first-order edges. In Section 4.5, a shape discriminating function is developed, and its response to different vessel shapes is analyzed. The above terms are integrated in the multi-scale framework to form a final vessel likelihood measure in Section 4.6.

4.1. Measure of brightness contrast

We first explore the usage of invariant K_1 in image structure detection. As mentioned before, K_1 is a measure of local volume change, it can also be verified to reflect relative density variation of material. By the mass conservation law, we obtain the derivative relation between material density ξ and volume V as $\xi \cdot dV + d\xi \cdot V = 0$, which can be easily transferred to $d\ \xi/\xi = -d\ V/V$. This means the relative increment of density is inverse to the concerned volume term. Considering an infinitesimal element of elastic solid with unit side length, and u_i being the components of deforming displacement $\vec{u}$, the volume changing ratio can then be approximated with

$$\lim_{\mathbf{V}\to\mathbf{0}} \frac{\delta \mathbf{V}}{\mathbf{V}} = \frac{\partial \mathbf{u}_1}{\partial \mathbf{x}_1} + \frac{\partial \mathbf{u}_2}{\partial \mathbf{x}_2} + \frac{\partial \mathbf{u}_3}{\partial \mathbf{x}_3}. \tag{11}$$

Here, δV indicates the volume increment and its limit is dV. According to mechanical theory, the right side of Eq. (11) is exactly the trace of strain tensor. Since the gradient of density is proportional to deforming displacement, we have $u_i \propto \frac{\partial \xi}{\partial x_i}$. Then, from Eq. (11), it is not difficult to derive

$$\lim_{\mathbf{V}\to\mathbf{0}} \frac{\delta \xi}{\xi} \propto -\left(\frac{\partial^2 \xi}{\partial \mathbf{x}_1^2} + \frac{\partial^2 \xi}{\partial \mathbf{x}_2^2} + \frac{\partial^2 \xi}{\partial \mathbf{x}_3^2}\right). \tag{12}$$

If the density ξ is assumed to be an image intensity I, Eq. (12) will explain that the local average intensity variation (i.e. contrast) can be measured with the Laplacian of image. Therefore, the invariant $K_1 = \sum_{i=1}^{3} \frac{\partial^2 I_\sigma}{\partial x_i^2}$ of Hessian tensor is able to work as an indicator of brightness contrast.

As a complement, the effect of invariant K_1 might be derived differently from the heat equation. When applied to image denoising, the heat equation is also called the homogeneous linear diffusion equation (Weickert, 1997), and takes the form of

$$\frac{\partial I}{\partial t} = \Delta I(t). \tag{13}$$

As well known, Eq. (13) is equivalent to Gaussian smoothing filter with $\sqrt{2t}$ being the scale σ (ter Haar Romeny, 2003). The corresponding time discrete equation is written as

$$I_{n+1} - I_n = \tau \Delta I_n, \tag{14}$$

and τ is a time step. Obviously, if $\triangle I_n < 0$, the local intensity value will decrease during iterations and vice versa . Notice the essence of heat equation is to describe the physical phenomena that the high density (intensity) mass or particles diffuse gradually to neighboring lower density regions. Thus, it can be considered as a contrast-driven diffusion with $\triangle I_n$ being the contrast strength at current scale. Based on the above analysis, we might define the scale-related Laplacian of intensity, i.e. $K_1 = \triangle I_\sigma$, as a measure of brigntness contrast. To some extent, this contrast term was used previously in the flux maximizing geometric flow (Vasilevskiy and Siddiqi, 2002) to generate a curve evolving speed for vessel segmentation.

Generally, we only need to confine the sign of K_1, with negative (positive) values corresponding to bright (dark) objects. For pulmonary CT images, we additionally choose a relative threshold in proportion to the maximum magnitude of eigenvalues (λ_m) to ensure noise immunity, i.e.

$$|K_1| = |\lambda_1 + \lambda_2 + \lambda_3| > 3\alpha\lambda_m. \tag{15}$$

Here, the proportional parameter α is adopted to adjust sensitivity, and its theoretical range is limited to [0,1) from the definition. The reason not to use an absolute threshold is that pulmonary vessels cover a large range of intensity variety, and it is difficult to balance the intensity gap between vessels with various sizes. It should be pointed out that this contrast constraint differs from the traditional ones, which only use the sign of the two eigenvalues with highest magnitude.

4.2. Measure of structure strength

The strain energy density is a term to quantify the local energy stored in a solid after mechanical loading. Based on the observation that stressed materials are in a compressed state similar to the intensity concentration of image structures, we attempt to develop a strain energy density function to evaluate structure strength.

For an isotropic and linear elastic material, the stress–strain relation without thermal effect is

$$\eta_{ij} = \frac{1+\nu}{\epsilon}\sigma_{ij} - \frac{\nu}{\epsilon}\delta_{ij}\sum_{k=1}^{3}\sigma_{kk}. \tag{16}$$

Here, ϵ and ν are Young's modulus and Poisson's ratio respectively, $\sigma_{ij}(\eta_{ij})$ the elements of stress (strain) tensor, and δ_{ij} the Kronecker delta function. Then, the strain energy density $\left(U = \frac{1}{2}\sum_{i=1}^{3}\sum_{j=1}^{3}\sigma_{ij}\eta_{ij}\right)$ can be rewritten as

$$U = \frac{1+\nu}{2\epsilon}\sum_{i=1}^{3}\sum_{j=1}^{3}\sigma_{ij}^2 - \frac{\nu}{2\epsilon}\sum_{k=1}^{3}\sum_{l=1}^{3}\sigma_{kk}\sigma_{ll}. \tag{17}$$

By diagonalization, we can also represent the density function in terms of the eigenvalues of the tensor:

$$U = \frac{1}{2\epsilon}(\lambda_1^2 + \lambda_2^2 + \lambda_3^2) - \frac{\nu}{\epsilon}(\lambda_1\lambda_2 + \lambda_1\lambda_3 + \lambda_2\lambda_3). \tag{18}$$

With the tensor decomposition in Section 3, the strain energy density function of the Hessian matrix can be defined as the combination of two orthogonal components, i.e.

$$U(H) = \frac{1-2\nu}{2\epsilon}(\overline{H} : \overline{H}) + \frac{1+\nu}{2\epsilon}(\widetilde{H} : \widetilde{H}). \tag{19}$$

The deduction is given in Appendix A. Essentially, Eq. (19) divides the energy density function into two independent parts: a volume changing (isotropic) energy and a distortion deforming (anisotropic) energy. Since ϵ does not affect the relative weights, we fix it to 0.5. To keep the value of $U(H)$ in the same power order as the original image intensity, the square root of strain energy density is adopted, i.e.

$$\rho(H) = \sqrt{(1-2\nu)(\overline{H} : \overline{H}) + (1+\nu)(\widetilde{H} : \widetilde{H})}. \tag{20}$$

Since $\overline{H}:\overline{H}=\frac{1}{3}K_1^2$ and $\widetilde{H}:\widetilde{H}=K_2^2$, Eq. (20) is actually a tensor invariant representation.

Before using $\rho(H)$, it is necessary to understand the physical meaning of Poisson's ratio v. In mechanics, when a sample of material is stretched in for example the horizontal direction, it tends to get thinner or larger in the vertical direction. The Poisson's ratio v is then defined as the ratio of vertical strain (relative displacement) to horizontal strain. This is actually a parameter to describe the mutual influence between deformations in different directions. For a stable material, the value range is $-1 \leqslant v \leqslant 0.5$. Based on the similarity of material deformation to intensity variation, it is possible to verify the effect of v in image processing. If $v < 0$, the intensity concentrating in one direction will cause the relative intensity increasing in the perpendicular directions, which is known to generate isotropic "blob" structures. Inversely, $v > 0$ will adversely affect the intensity concentration in orthogonal directions, and then encourage anisotropy. Actually, the above relation can be easily checked from the two weights of isotropic and anisotropic energy terms in Eq. (20) by taking different v values. If $v = 0$, $\rho(H)=\sqrt{\lambda_1^2+\lambda_2^2+\lambda_3^2}$, which is then the "second-order structureness" first used by Frangi et al. (1998). Here, we point out that v is adjustable to the requirement of applications.

To verify the effect of v on real images, we illustrate a vessel likelihood function which will be elaborated later in Eq. (31). Here, the Poisson ratio varied from -1.0 to 0.5, while the remaining parameters were kept fixed, i.e. $\alpha = 0.1$, $\beta = 0.06$, $\kappa = 0.5$. An individual vessel tree was selected for demonstration. The original image is visualized in Fig. 1a. The performance with varying v can be observed in Fig. 1b–d. For brevity, we only show the three representative results, i.e. $v = -1.0, 0.0, 0.5$. As illustrated, a negative v tends to smoothen branches, but the junctions deteriorate with decreasing v, even disconnections occur around the bifurcations (labeled with green circles). Inversely, anisotropic structures are commonly enhanced by positive v values. This can be seen not only from the obviously strengthened vascular junctions, but also from the newly visible weak branches after filtering (see the blue[1] circles). But a high positive v may lead to coarse surfaces and degrade some irregular vessel structures, e.g. the blob-like deformations (indicated with red circles) will be exaggerated and tend to be broken. Therefore, the parameter v essentially acts to adjust the sensitivity to anisotropy.

4.3. Intensity continuity constraint

Most vessel structures including the branch, junction and crossing, share one common characteristic: there exists at least one direction in which the intensity variation is very small. This intensity continuity constraint has been used widely in various vessel detection techniques (Qian et al., 2009).

Although in real vascular images, the continuity constraints are often violated due to noise corruption, it can still be observed at an appropriate scale σ. The intensity continuity constraint at pixel x_0 in direction $\vec{r}$ is equivalent to $I_\sigma(x_0+h\vec{r})-I_\sigma(x_0)\approx 0$, with $\vec{r}$ a unit vector and h the magnitude. Then, the corresponding Taylor expansion is

$$\nabla I_\sigma(x_0)\cdot\vec{r}+\frac{h}{2}\vec{r}^{t}H_\sigma(x_0)\vec{r}\approx 0. \tag{21}$$

If the edge (first-order derivative) dominates the location, we can use $\nabla I_\sigma(x_0)\cdot\vec{r}\approx 0$ to find the vessel orientations. This is essentially the theoretical basis behind gradient-based vessel detecting techniques (Agam et al., 2005). Instead, if the first-order derivative is negligible, the Hessian term will mainly account for the intensity variation, i.e.

$$\vec{r}^{t}H_\sigma(x_0)\vec{r}\approx 0. \tag{22}$$

To investigate the influence of intensity continuity on Hessian eigenvalues, we first decompose $\vec{r}$ in the coordinate system of eigenvectors:

$$\vec{r}=c_1\vec{e}_1+c_2\vec{e}_2+c_3\vec{e}_3. \tag{23}$$

As elaborated in Appendix B, the eigenvalue representation is obtained as

$$\vec{r}^{t}H_\sigma(x_0)\vec{r}=c_1^2\lambda_1+c_2^2\lambda_2+c_3^2\lambda_3. \tag{24}$$

Then, from Eq. (22), we have

$$c_1^2\lambda_1+c_2^2\lambda_2+c_3^2\lambda_3=0. \tag{25}$$

Since none of the above coefficients (c_i^2) are negative, it can be inferred that only two conditions of eigenvalues distribution are able to satisfy Eq. (25):

- At least one of the eigenvalues (e.g. λ_i) is zero. Thus, with $c_i^2=1$ and other coefficients nulls, the sum on the left side will be 0.
- The eigenvalues take different signs, e.g. a positive eigenvalue and two negative ones. If they are all positive or negative, the weighted sum will never be 0.

The first condition occurs where the intensity continuity directions coincide with the eigenvectors, which includes the line (one zero eigenvalue) and sheet (two zero eigenvalues) structures. The homogeneous region has full zero eigenvalues and is continuous in all directions. The second condition corresponds to more general cases, where the intensity similarity results from the interaction of compression (intensity increasing) and expansion (intensity decreasing) in varying eigenvector orientations. Particularly, it is able to explain the eigenvalue distribution of vessel junctions, which have intensity continuity directions different from the eigenvectors, and even perhaps have more than one continuity directions. This condition also conforms to the eigenvalue distribution of vascular stenoses described previously by Sato et al. (2000).

4.4. Relative Hessian strength

The above second-order structure analysis is established on the assumption that the gradient term in Eq. (21) is relatively weak compared to the Hessian component. We emphasize that it is nontrivial to quantify the relative strength of the second-order derivatives, and ensure its dominance over the gradient. Since the gradient magnitude is defined as the maximum response of $\nabla I_\sigma(x_0)\cdot\vec{r}$, we define the magnitude of Hessian matrix as

$$\|H\|_\infty=\max\{|\vec{r}^{t}H\vec{r}|,\quad \|\vec{r}\|=1\}. \tag{26}$$

Substituting Eq. (24) into Eq. (26), we can find that $\|H\|_\infty$ is the maximum magnitude of eigenvalues, i.e. λ_m. Then, a relative Hessian strength function can be defined as

$$G_{rel}(x)=\exp\left(-\beta\frac{\|\nabla I\|}{\lambda_m}\right). \tag{27}$$

Here, the constant $\beta > 0$ is used to adjust the sensitivity of response. $G_{rel}(x)$ will tend to 1, while $\lambda_m \gg \|\nabla I\|$. Conversely, it will take value of 0, while $\lambda_m \ll \|\nabla I\|$. This relative strength function is useful in suppressing step-edges, which also respond strongly to eigenvalue detection like the second-order structures, but take strong gradient (Koller et al., 1995; Lorenz et al., 1997). Another potential effect of this term is to prevent small objects from being overlapped by larger smoothing kernels (Agam et al., 2005; Bennink et al., 2007),

[1] For interpretation of color in Figs. 1, 2, 4–8, the reader is referred to the web version of this article.

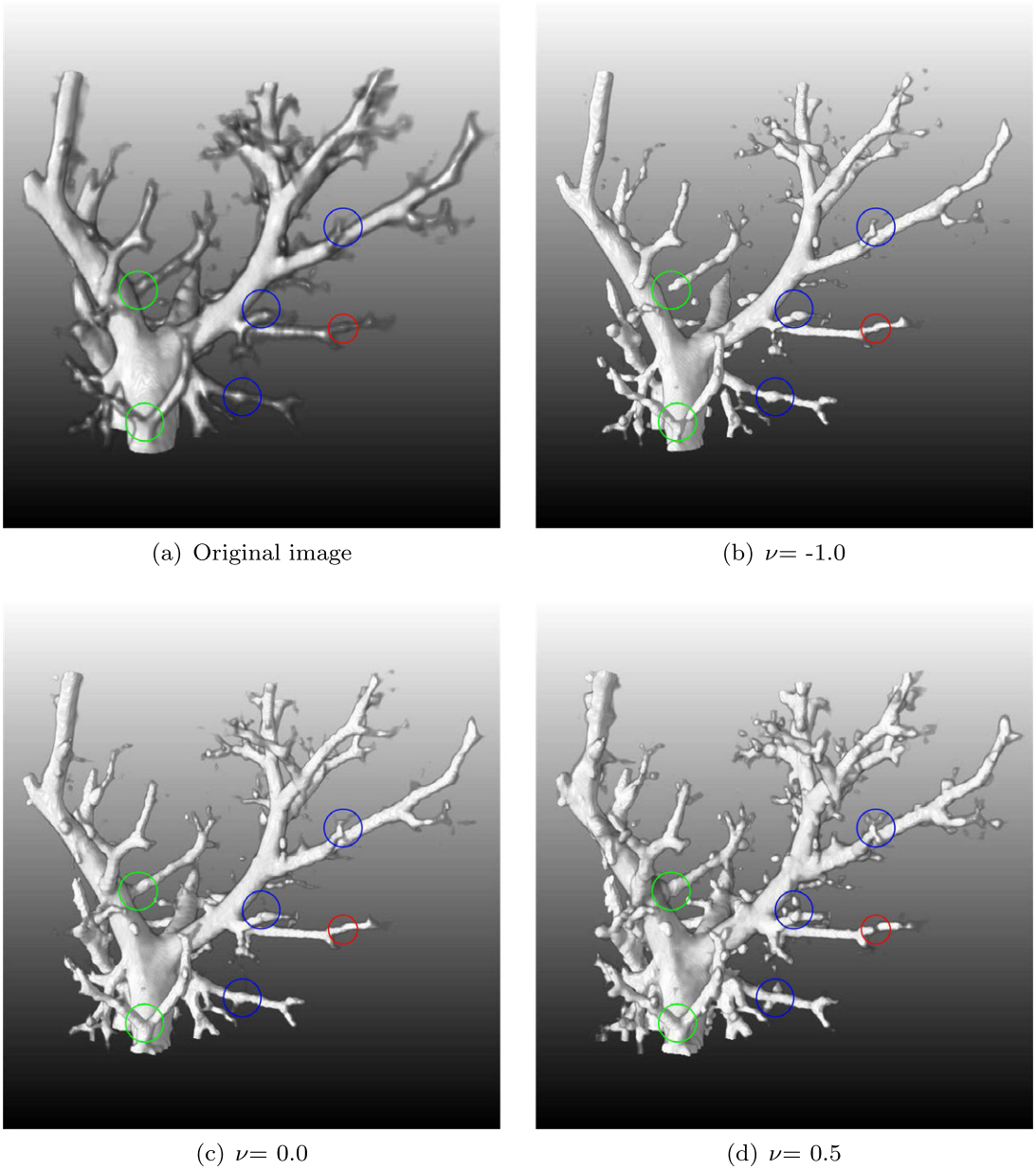

(a) Original image (b) ν= -1.0

(c) ν= 0.0 (d) ν= 0.5

Fig. 1. Comparing results of the proposed filter with varying parameter v.

since the blurred boundaries appear to have low Hessian strength. Recently, Bauer et al. (2010) presented a similar step-edge suppressing term to adaptively adjust medialness response near vascular boundaries.

4.5. Vessel shape discrimination

Until now, we only discussed the detection of common second-order structures. It is important to design a specific shape discrimination function for vascular images. In this paper, we follow the tensor "shape" concept of traditional vessel filters by evaluating the relative magnitude change of Hessian eigenvalues, while neglecting the orientation of its eigenvectors.

As mentioned in Section 3, the invariant K_3 is termed *mode* by Criscione et al. (2000) in a continuum mechanics context. Intrinsically, the *mode* is a dimensionless parameter of anisotropy type, varying between -1 and +1. Ennis and Kindlmann (2006) verified its effect in distinguishing planar and linear anisotropy of diffusion tensor. However, the shape discriminating ability of *mode* will gradually decrease when the anisotropy of structures becomes weaker. To remedy this drawback, we introduce the fractional anisotropy (*FA*) as an additional indicator.

Fractional anisotropy was originally proposed by Bassera and Pierpaoli (1996), and has been widely used in diffusion tensor imaging. Since the Hessian matrix is not necessarily positive-definite as diffusion tensors, we modified the original formulation by multiplying with a different constant:

$$FA = \sqrt{3\frac{\widetilde{H} : \widetilde{H}}{H : H}} = \sqrt{\frac{(\lambda_1-\lambda_2)^2+(\lambda_1-\lambda_3)^2+(\lambda_2-\lambda_3)^2}{\lambda_1^2+\lambda_2^2+\lambda_3^2}}. \tag{28}$$

This ensures that $FA = 1$ for an ideal vessel branch ($|\lambda_1| \approx 0$ and $\lambda_2 \approx \lambda_3 \gg 0$ or $\ll 0$). Since $\widetilde{H} : \widetilde{H} = K_2^2$ and $H : H = \frac{1}{3}K_1^2 + K_2^2$, FA can also be considered as a relative ratio between the invariant K_1 and K_2. In addition, the eigenvalue representation of *mode*(K_3) is

$$mode(x) = \sqrt{2}\frac{\frac{1}{3}\sum_{i=1}^{3}(\lambda_i - \bar{\lambda})^3}{\left(\frac{1}{3}\sum_{i=1}^{3}(\lambda_i - \bar{\lambda})^2\right)^{\frac{3}{2}}}, \quad (29)$$

with $\bar{\lambda}$ the average eigenvalue. Although both *FA* and *mode* can be computed without eigenvalue decomposition, the above expressions are useful for intuitive understanding of their responses to varying vessel structures.

To investigate the potential of *FA* and *mode* in discriminating vessel shapes, we need to know not only their values on specific vessel structure, but also their response curves concerning the transition between various structures. Based on the previous intensity continuity constraint, the eigenvalue distributions of typical vessel structures including the vessel branch, boundary, junction (or stenosis), blob and step-edge, are summarized in Table 1. Since the vessel branch (usually considered as a line or tubular shape) is the standard structure, the shape deviation (transition) of other structures from the ideal branch is described with the change of one eigenvalue (shown as column 3 in Table 1). Here, we consider only bright objects, set $\lambda_3 = -\lambda_m$ to be the maximum magnitude eigenvalue, and other eigenvalues are represented in relative ratio to λ_m. Without loss of generality, the tolerance of the remaining third eigenvalue is considered, and the variation range is set to $\frac{1}{2}\lambda_m$ as shown in column 4. The novelty of this classification is that we use two negative eigenvalues and one comparatively smaller positive eigenvalue to represent non-tubular vascular structures (labeled as junction and stenosis here). In our category, Types *I*–*III* are initialized from the line shape, and one exception (Type *IV*) is originally the extensive part of Type *II*. The corresponding 3D curves of *FA* and *mode* are shown in Fig. 2.

According to the distribution of eigenvalues, we divide the shape transitions into two groups: low-anisotropy and high-anisotropy. The weak anisotropy group ($FA < 1$) corresponds to "Type *I*". As observed, the *mode* curves vibrate unstably with isotropy increasing ($\lambda_1 \approx -\lambda_m$). But *FA* decreases gradually from 1 to 0 with the shape deviating from the ideal branch, and is then able to act as a discrimination function. The effect is equivalent to the "blob" suppressing term used in traditional Hessian filters. The high-anisotropy group ($FA \geqslant 1$) contains the remaining three types. Since *FA* is only a measure of anisotropy strength, its shape selecting ability will become invalid here. Instead, the *mode* of anisotropy is effective now. For "Type *II*", the transition from vessel branch center to boundary is indicated. We can find that the *mode* curve occurs to be a quadratic descending function, which will work as a "sheet" suppressing term. Furthermore, the most attractive characteristic of anisotropy *mode* is shown in "Type *III*". Here, the curve responds with the same high value close to 1 for all structures including line, junction and stenosis. This means the *mode*, as a shape discriminating parameter, will accommodate local deformations from normal vessel branches, and help to solve the problem of junction suppression. However, *mode* is not as good in suppressing step-edges as its performance on sheet structures (see "Type *IV*" in Fig. 2). It is known that the second-order derivative operator often gets strong response on step edges (Koller et al., 1995). But this problem is believed to be well compensated in our model by the "relative Hessian strength" and "brightness contrast" terms mentioned before, because the step-edges usually have strong gradient and low average eigenvalue.

From the above analysis, we formularize the final vessel shape discriminating function as

$$V(x) = \begin{cases} \sqrt{FA}, & FA < 1 \\ \frac{1}{2}[mode(x) + 1], & \text{otherwise} \end{cases}, \quad (30)$$

where the *mode* term is modified to limit its value inside [0, 1], and the square root of *FA* is adopted to balance the curve tendency, then makes both "blob" and "sheet" shapes be equivalently suppressed under the same discriminating function.

4.6. Multi-scale vesselness measure

The strain energy density function $\rho(H)$ in Eq. (20) has no shape selecting ability. Therefore, we multiply it with $V(x)$ to form a shape-tuned function, and the relative Hessian strength is weighted to suppress undesired first-order structures. Further considering the brightness contrast constraint, our final weighted density function is presented as

$$\varphi(\sigma, x) = \begin{cases} 0, \text{if } \frac{1}{3}(\lambda_1 + \lambda_2 + \lambda_3) > -\alpha\lambda_m \\ \exp\left(-\beta\frac{\|\nabla I\|}{\lambda_m}\right)V^{\kappa}(x)\rho(H, \nu), \text{else}. \end{cases} \quad (31)$$

The maximum eigenvalue magnitude λ_m and parameters α, β,ν are the same as defined previously. A power coefficient $\kappa > 0$ of $V(x)$ is added to adjust the sharpness of shape selectivity. Theoretically, κ could be any positive value, but a high one ($\kappa > 1$) will become very sensitive to shape deviation. Here, we only consider the case of bright objects and dark background. It is trivial to formulate the inverse cases.

The scale related first- and second-order derivatives are computed by convoluting with Gaussian operators, where the γ-normalization (Lindeberg, 1998) is adopted to compensate intensity decrease due to smoothness. For comparing across scale space, the weighted strain energy density at each discrete scale is re-scaled to [0,1] with $\bar{\varphi}(\sigma, x)$ being the normalized function. Presently, the rescaling operation is implemented by dividing by the maximum of $\varphi(\sigma,x)$. The traditional multi-scale framework can be utilized to generate the maximum response of vessels with various sizes:

$$\varphi_m(x) = \max\{\bar{\varphi}(\sigma, x), \sigma_{\min} < \sigma < \sigma_{\max}\} \quad (32)$$

where $\sigma_{\min}$ and $\sigma_{\max}$ are the selected minimum and maximum scales. Thus, $\varphi_m(x)$ is similar to a vesselness function (Frangi et al., 1998), which measures the likelihood that a voxel belongs to a blood vessel in the original image.

5. Experiments and evaluation

Our algorithm was implemented in the C++ language, using the ITK package (Ibáñez et al., 2005). The calculation time for a typical $512 \times 512 \times 80$ size dataset is about 20 s for a single scale on our

Table 1
Eigenvalue distribution and transition between typical vessel structures.

Type	Initial structure	Transition	Tolerance	Final structure
I	Vessel branch (line) $\lambda_1 = 0, \lambda_2 = -\lambda_m, \lambda_3 = -\lambda_m$	λ_1:0 → $-\lambda_m$	$\lambda_2 \in [-\frac{1}{2}\lambda_m, -\lambda_m]$	Blob $\lambda_1 = \lambda_2 = \lambda_3 = -\lambda_m$
II		λ_2:$-\lambda_m$ → 0	$\lambda_1 \in [-\frac{1}{4}\lambda_m, \frac{1}{4}\lambda_m]$	Vessel boundary (sheet) $\lambda_1 = \lambda_2 = 0$, $\lambda_3 = -\lambda_m$
III		Junction and stenosis		
		λ_1:0 → λ_m	$\lambda_2 \in [-\frac{1}{2}\lambda_m, -\lambda_m]$	Symmetric stenosis $\lambda_1 = \lambda_m$, $\lambda_2 = \lambda_3 = -\lambda_m$
IV	Vessel boundary (sheet)$\lambda_1 = \lambda_2 = 0$, $\lambda_3 = -\lambda_m$	λ_2:0 → λ_m	$\lambda_1 \in [-\frac{1}{4}\lambda_m, \frac{1}{4}\lambda_m]$	Step edge $\lambda_1 = 0$, $\lambda_2 = \lambda_m$, $\lambda_3 = -\lambda_m$

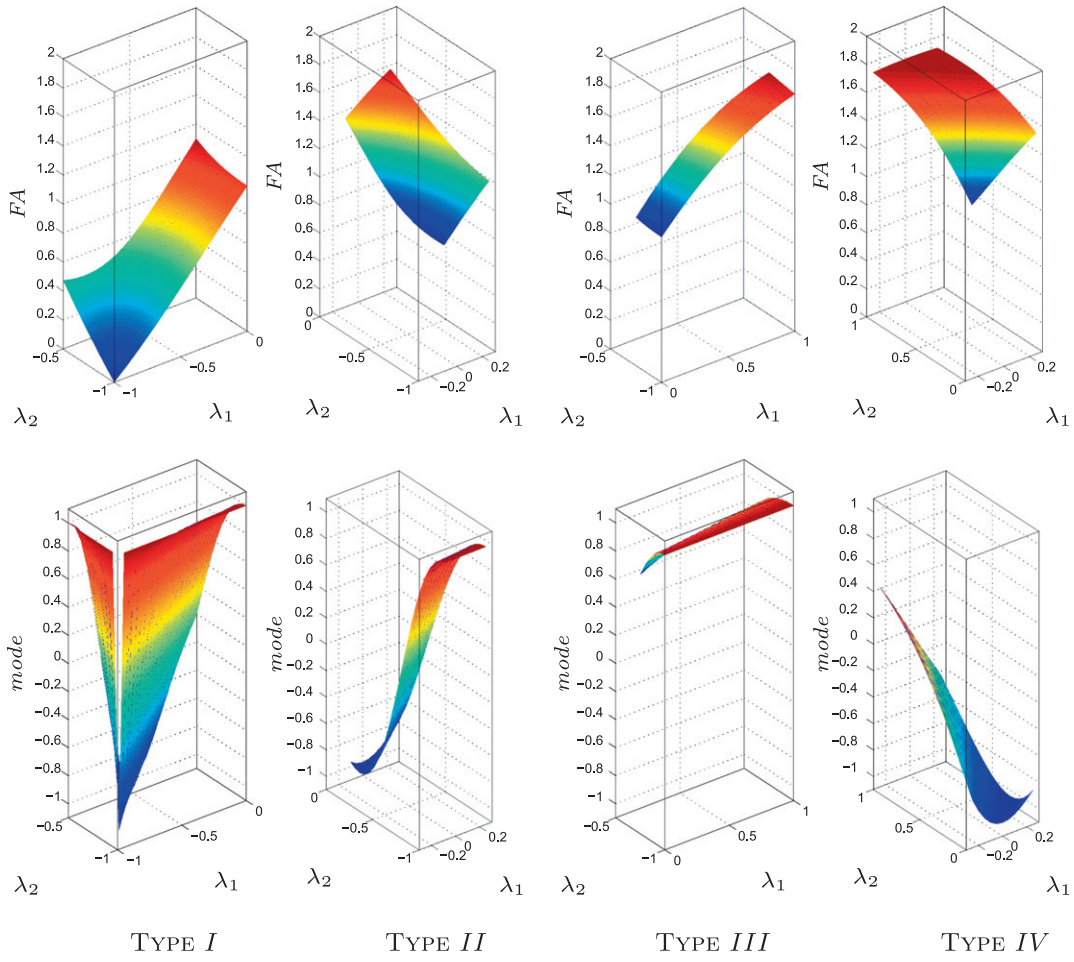

Fig. 2. Responses of *FA* and *mode* to various vessel structures. The Type *I–IV* curves corresponding to Table 1 are arranged orderly from left to right, and we plotted the 3D *FA* and *mode* surfaces separately in the upper and lower rows.

computer, configured with 2.66 GHz CPU and 3 GB memory. The computing speed is expected to increase largely with multi-threading and parallel programming.

5.1. Data and evaluation methods

We evaluated the proposed method on synthetic and clinical datasets. For the synthetic data, a digital phantom was generated by modeling with 3ds Max (Autodesk Inc.), and then discretized into $225 \times 153 \times 18$ size images. As shown in Fig. 3a, six objects were created to simulate different kinds of vessel structures, which resemble stenoses, varying diameter, bifurcations, curved and touching branches, respectively. Furthermore, the intensity profile was idealized as a Gaussian function of distance to the boundary. Setting the background to one-third of the maximum intensity, synthetic images were produced by adding multiplicative Gaussian noise with different variances. Thus, Fig. 3a is the ground truth.

The clinical data were acquired of two patients in the supine position on a Toshiba Aquilion 16 detector row CT scanner without contrast media. The images were reconstructed at a 0.5 mm slice thickness with a 0.5 mm slice increment. The in-plane voxel size was set to 0.7×0.7 mm, and an FC02 reconstruction filter was used.

Unlike the synthetical data, no gold standard existed in advance for the clinical images. Artificially defined references were used in our validations. Due to the complexity of pulmonary vessels, manual segmentation is extremely tedious and time-consuming. It is unrealistic to artificially extract the vessel network of a whole lung. Instead, we randomly chose sub-volumes of the CT images across the boundary of pulmonary lobes, where the bright plane-shaped fissure (a fiber tissue between lung lobes) and plenty of vessel details make it a challenging region. Subsequently, a technical expert and a pulmonologist were asked to hand-draw the data, using the interactive tools of ITK-snap (Yushkevich et al., 2006). Then, a thorax surgeon was enquired for further verification. A final segmentation is shown in Fig. 4b, and will serve as reference standard in the quantitative evaluation. Here, the red surfaces indicate the vessels, the blue ones represent bronchi, and green plane is the fissure. In total, two "reference standards" corresponding to two different patient data were extracted, which will be exchanged for training and testing (i.e. cross-validation) in our experiments.

Our results were compared with three traditional Hessian-based filters (Frangi et al., 1998; Sato et al., 1997; Li et al., 2003), whose implementations were downloaded from the ITK package and Insight Journal (Antiga, 2007; Enquobahrie et al., 2007), and the different kinds of vessel likelihood were considered. Here, we only adopted the early method of Sato et al. (1997), which is now a standard ITK filter. The stenosis preservation was addressed in their improved version (Sato et al., 1998). Both visual and quantitative evaluation methods were adopted for comparison. The 3D visualizations were implemented with the standard modules in Mevislab (Bitter et al., 2007), and the rendering parameters were kept consistent among the same type of images.

The quantitative evaluations were conducted by plotting the *precision–recall* (*PR*) curve after binarizing the filtered images with varying global thresholds. The *PR* curve was reported to perform

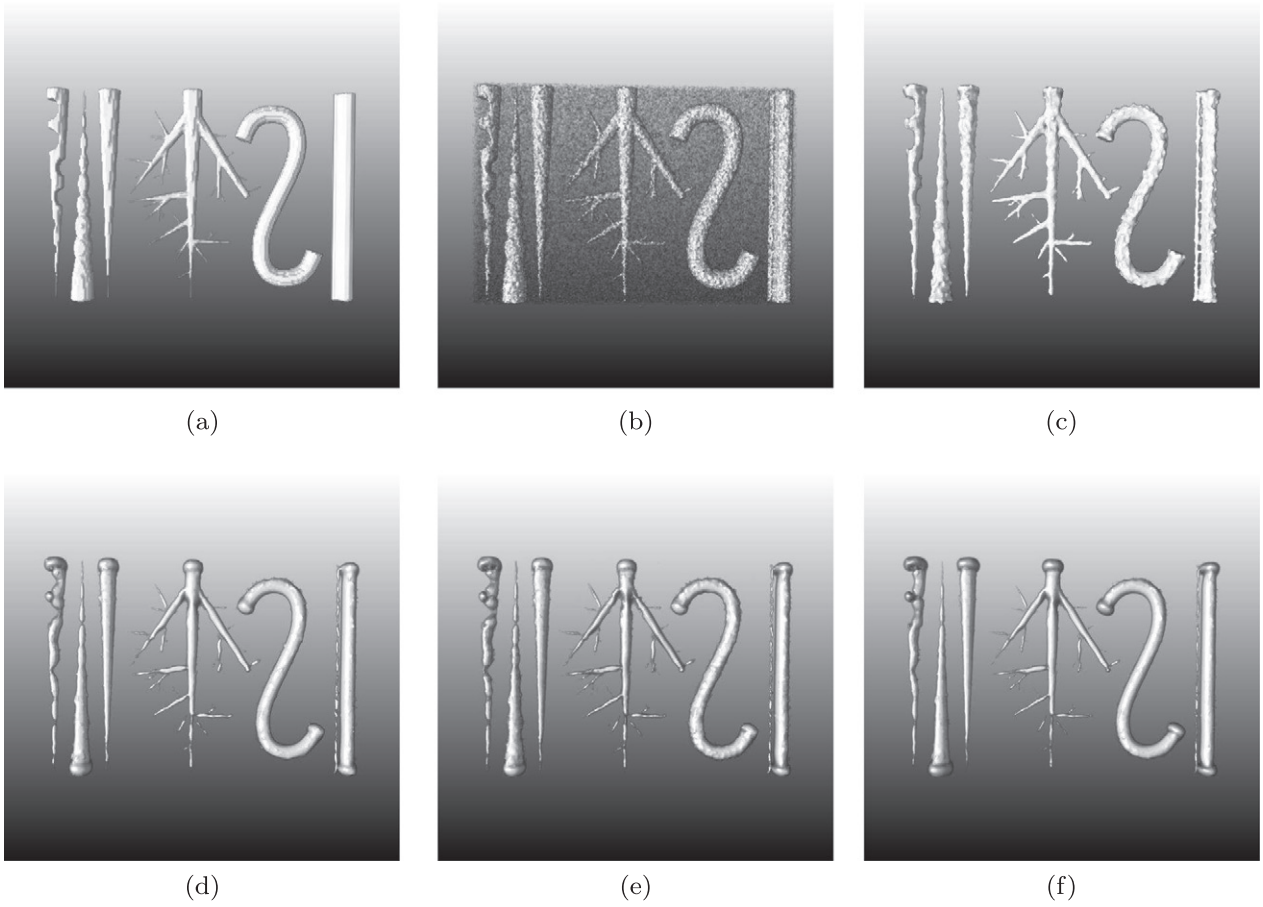

Fig. 3. Synthetic dataset experiment. (a) Original image; (b) synthetic image corrupted with 16% variance Gaussian noise; (c)–(f) are respectively the enhanced images of our method, Frangi, Li and Sato filters.

better than the Receiver Operator Characteristic (ROC) curve in assessing the classifying problems like vascular images, where the number of negative sample (background) greatly exceeds the positive sample (object) (Davis and Goadrich, 2006). Here, the *precision* indicates the percentage of detected objects that are truly vessels, the *recall* (sensitivity) corresponds to the ratio of true vessels that have been detected correctly. We defined two different kinds of *recall* namely in terms of volume and skeleton. The latter is implemented by checking the overlap between the centerline of "ground truth" and the extracted vessel body. It is not difficult to understand that this implementation will emphasize the presence of vessels but neglect their radial size. Actually, the size and boundaries are often uncertain for a vessel with a Gaussian profile. Therefore, the skeleton-based *recall* will be sensitive to the connectivity of vascular network, which is mainly influenced by the preservation of bifurcations and thin vessels. Usually, the area under curve (AUC) of the *PR* curves are calculated to give an overall evaluation. To distinguish the above volume and skeleton related *precision–recall* curves, we name them separately as PR_v and PR_s. Correspondingly, the area terms are AUC_v and AUC_s.

5.2. Optimization of parameters

There are four vessel filters used in our experiments. In order to compare the best possible results of all the methods, we optimize their parameters on various types of data. No parameters are involved in the Li et al. (2003) filter. The fixed parameters of Sato et al. (1997) and Frangi et al. (1998) filters are set the same as the original papers, then only the noise-suppressing parameter c of Frangi method need optimizing.

The proposed method has four parameters. Among them, the shape selective parameter κ is empirically set inside [0.3, 0.8] with 0.5 being a reference value for real vessels, and it can be further adjusted according to the specific property of objects. Generally, a lower κ tends to loose the restriction of "sheet" and "blob" deformations. The choice of v is also application dependent. In pulmonary images, we prefer a positive v owing to the importance of preserving vascular connectivity at bifurcations. In our experiments, a positive value $0.1 < v < 0.3$ is sufficient to satisfy the requirement of junction enhancement in most cases. It is safe to set $v = 0$, if no priority of structures is involved.

The remaining parameters α and β may be manually adjusted by gradually increasing values from 0. Since the effect of β is to adjust the strength of suppressing first-order edges, and α accounts for the sensitivity to noise, both of them will tend to remove weak structures and thin vessels if too large values are adopted. For vascular images, the empirical configuring ranges are $\alpha \in [0, 0.4]$ and $\beta \in [0, 0.4]$. While the ground truth or reference standard is available, the two parameters can be optimized automatically based on the *PR* measure. Generally, the best parameters are chosen where the sum of normalized AUC reaches its maximum. We demonstrate this by using the first clinical data in Section 5.4. The AUC_v and AUC_s responses to varying α and β are calculated and generate the color filling contour graphs in Fig. 5a and b. Then, the AUC functions are normalized by dividing by their maxima. The maximum of their rescaled sum is located at $\alpha = 0.20$ and $\beta = 0.06$, which are chosen the optimized values.

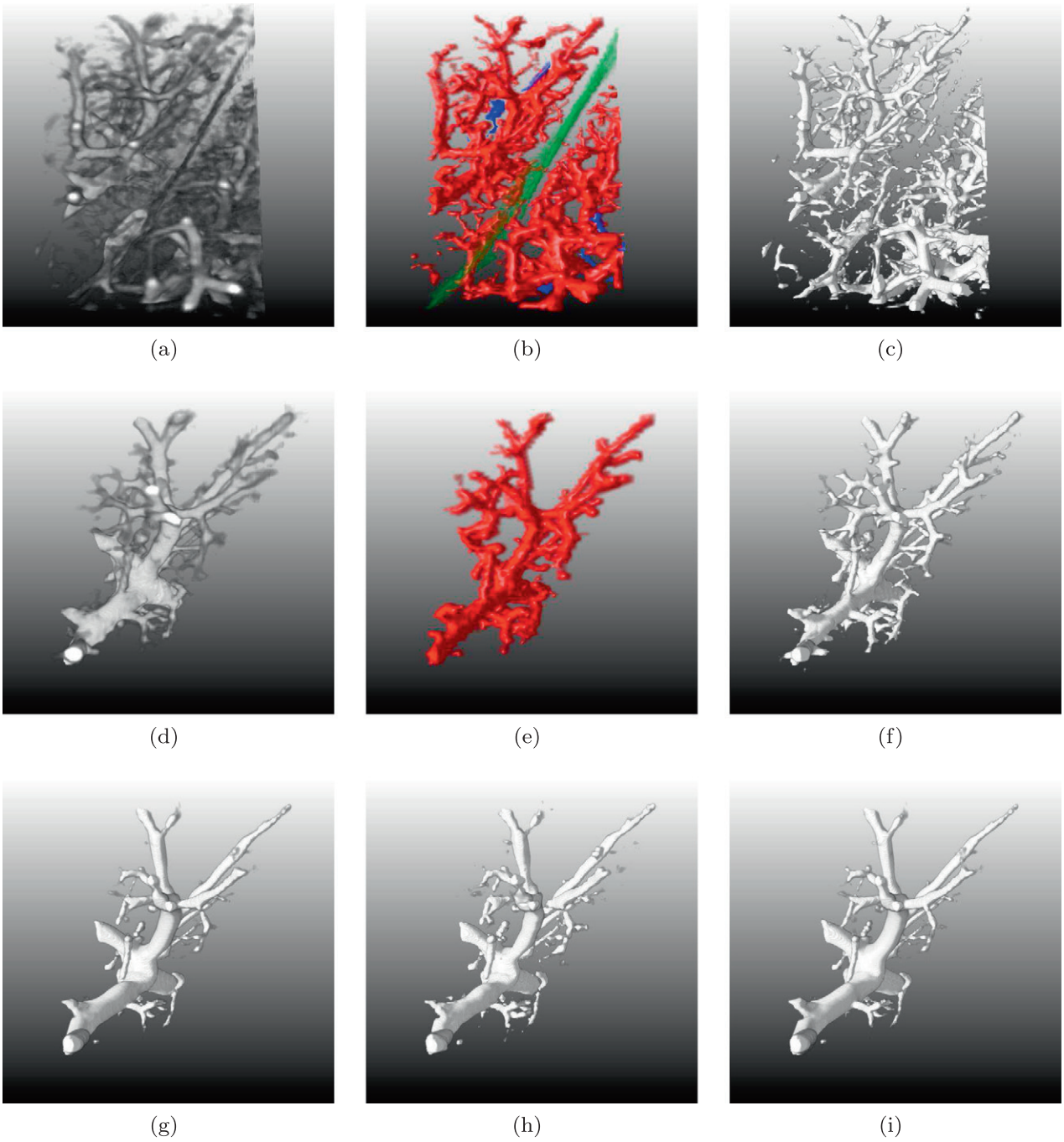

Fig. 4. The first non-contrast-enhanced pulmonary CT dataset experiment. (a) original image; (b) manually segmented reference standard; (c) filtered image of our method; (d)–(i) are the extracted ROI from the original image, reference standard, the filtered results of proposed, Frangi, Li and Sato method, respectively.

Similarly, the noise-suppressing parameter c of Frangi's filter was also optimized automatically with the corresponding AUC responses as shown in Fig. 5c. It can be seen that AUC_v and AUC_s do not reach their extreme values simultaneously. Then, the maximum of the normalized sum is also used to find the optimized parameter, and we have $c = 120$.

5.3. Synthetic dataset experiment

We compared the four filters on the synthetic image with 16% variance noise in Fig. 3b. The scale range used in this experiment is 1–6 pixels, and is further divided logarithmically into 10 steps. According to Section 5.2, our parameters were optimized to $\alpha = 0.2$ and $\beta = 0.02$. Considering the complexity of phantom shapes, we chose a smaller shape selecting parameter ($\kappa = 0.4$) than the reference value to accommodate more deformation. v was simply set to 0 without priority to specific structures. Similarly, we optimized the parameter c of Frangi's filter to 0.65. Here, the synthetic image was in its original float type with low pixel values, which lead to a smaller c compared with the clinical data. The filtering results are given in Fig. 3c–f. As shown, the traditional Hessian filters were not good to preserve the junctions and local deformations, where disconnections in varying degrees can be observed. The distortions near the endpoints of cylinders can be considered as a reflection of the wrong response to step-edges. The proposed method has more advantages in enhancing both vascular

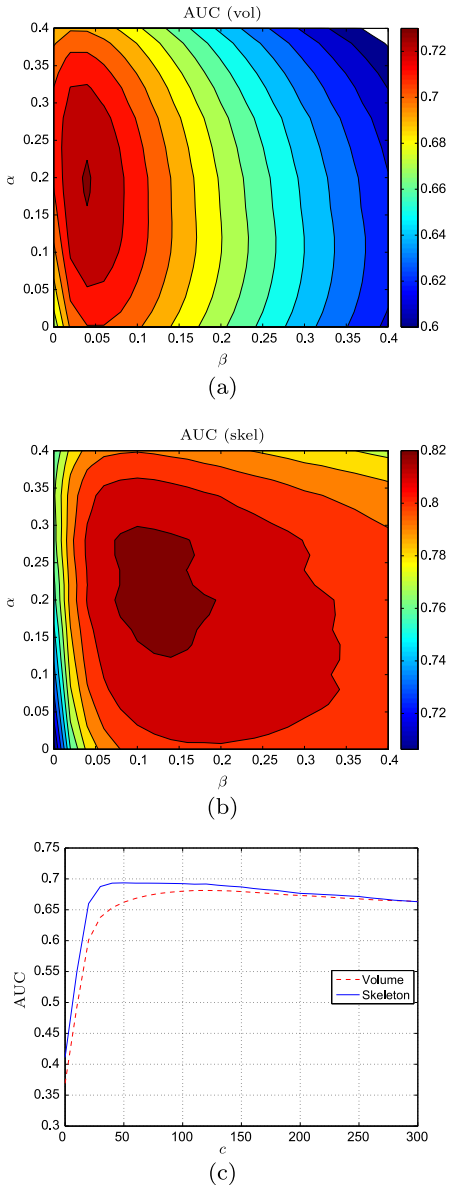

Fig. 5. Optimization of parameters on the first clinical data. (a) and (b) are respectively the AUC responses of PR_v and PR_s curves with the proposed filter ($\kappa = 0.5, v = 0.1$), where the steps of contour level are fixed to 0.01; (c) is the corresponding response of Frangi's filter.

branches and bifurcations. Additionally, most details including local diameter variety and thin vessels are well preserved. The merit of our method in preserving details and separating touching branches (see the rightmost objects in Fig. 3c) is partly ascribed to the first-order structure suppressing ability of the relative Hessian strength term. However, over-suppression will weaken the vessel boundaries and make the diameters look smaller. Another shortcoming may be that our method tends to develop coarser surfaces, which arises from the difficulty in balancing between smoothness and the sensitivity to details.

The quantitative evaluation continues by plotting the *PR* curves in Fig. 6a and b. For PR_v, the proposed method performs almost the same as Frangi filter. But our advantage is obvious with the PR_s measure, which can be clearly checked with the AUC_s given in the legend of the figure. Since *precision* can be seen as a measure of exactness or fidelity and *recall* a measure of completeness, the proposed method is considered to have detected more true vessels (in terms of presence) with the same fidelity level. Essentially, the advantage shown in Fig. 6b just reflects the performance of our method in preserving bifurcations and thin vessels, which directly contribute to the better completeness of vessel topology. To check the immunity to noise, we further tested these filters on a series of synthetic images with different noise levels, while the filtering parameters were kept the same as Fig. 6b. The corresponding AUC_s curves are plotted in Fig. 6c. As observed, the proposed method appears to be more stable to noise.

5.4. Clinical dataset experiment

Our method was further validated by using two clinical datasets, which work mutually as training and testing sets. Since the manually extracted reference standards are available, we were able to optimize the filtering parameters as described in Section 5.2. Two different configurations of parameters were obtained for Frangi and the proposed filters.

The contrast and edge-suppressing parameters of the proposed filter were automatically optimized to $\alpha = 0.2$ and $\beta = 0.06$ (labeled as "Our method1") on the first dataset, and $\alpha = 0.22$, $\beta = 0.1$ ("Our method2") for the second one. In both configurations, we manually chose a default $\kappa = 0.5$, and a positive $v = 0.1$ to enhance junctions, since image intensity usually decreases around vessel bifurcations (Verschakelen and Wever, 2007). Simultaneously, the noise-suppressing parameter of Frangi's filter was automatically optimized to $c = 120$ ("Frangi1") and $c = 90$ ("Frangi2") for the first dataset and the second dataset , respectively. The selected vascular scales were 0.5–3.0 mm, and 10 steps were used for all the four vessel filters.

We selected a sub-volume of data for validation as described in Section 5.1. With Fig. 4a and b being the original image and reference standard from the first pulmonary CT data, the result of our method is presented in Fig. 4c. Compared with the reference standard, the fissure (rendered in green with low opacity) is basically invisible in our result, which just verified the ability of the proposed method in suppressing unwanted sheet (plane) structures. For better observation of details, an independent vascular tree in Fig. 4d was extracted and visualized. Fig. 4f–i shows the corresponding ROIs from the results of the four filters. As illustrated, although the main large vessel branches are well preserved with the three traditional methods, the weakening and missing of junctions are commonly seen, especially in places where small vessels link to a larger branch. Our result appears to contain most vascular trees, both branches and bifurcations are enhanced without distortion. In particular, thin vessels and local deformations are clearly preserved and connected to main vessels. This will be a useful feature for pulmonary lobe segmentation, because the extraction of complete and unbroken vessel network will directly benefit the estimation of the lobe position (Kuhnigk et al., 2003; Ukil and Reinhardt, 2009).

The *PR* curves are also plotted to quantitatively evaluate the filtering performance. Since the reference standard was drawn manually, it is inevitable that some fine vessels may not be accurate and the vascular boundaries appear coarse and irregular. But the local uncertainties are believed not to affect the global evaluation, particularly to determine the presence of vessels. The computed curves of the first clinical image are shown in Fig. 7. As observed, the proposed filter takes the maximum AUC for both PR_v and PR_s, especially obvious with the latter. Different from the synthetical image experiment, the performance of the proposed method is clearly better than other filters in the volume-based evaluation. This may be ascribed to the fact that real edges in clinical image are not so sharp as the idealized ones in phantoms, thus the step-edge suppressing term will not cut down too much vascular region. In Fig. 7b, the recalls of our method are higher than the other methods at almost all precision levels. This is consistent with

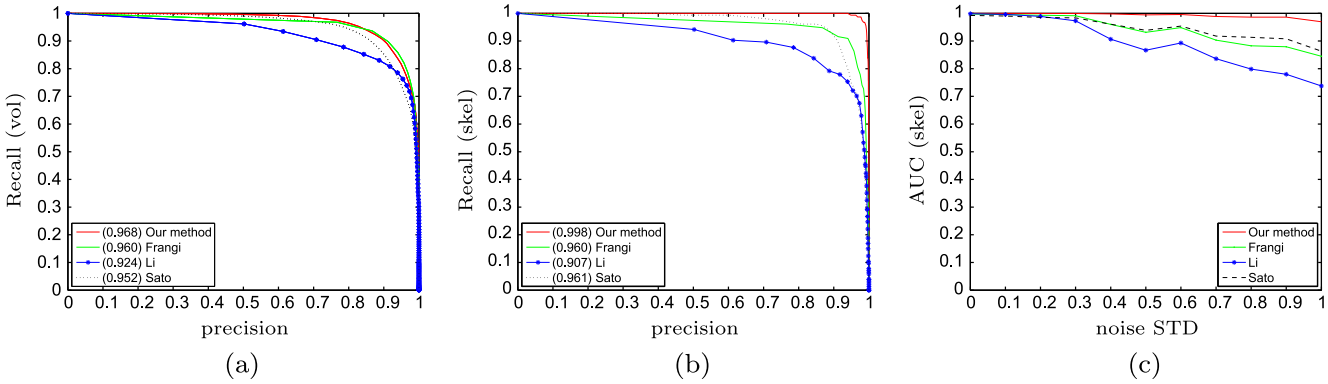

Fig. 6. Quantitative evaluation of filtered synthetic images with *PR* curves. (a) and (b) respectively correspond to the PR_v and PR_s, and the numbers inside the brackets of legend are AUC values. (c) indicates the change of AUC_s to varying standard deviations of Gaussian noise.

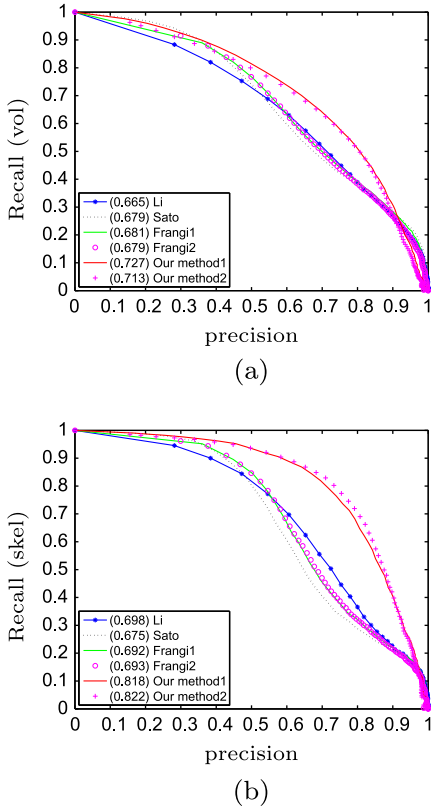

Fig. 7. Quantitative evaluation of the first pulmonary image filtering with *PR* curves. (a) and (b) respectively correspond to the PR_v and PR_s, where the numbers inside the brackets of legend are AUC.

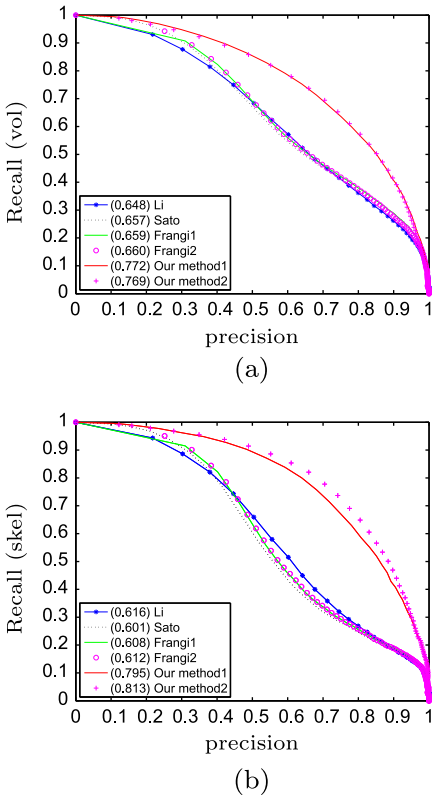

Fig. 8. Quantitative evaluation of the second pulmonary image filtering with *PR* curves. (a) and (b) respectively correspond to the PR_v and PR_s, where the numbers inside the brackets of legend are AUC.

the visual illustration, where our filtered image contains more small vessels as well as feature details. Therefore, in terms of connectivity and completeness of the detected vessel tree, the proposed method outperformed the other filters.

To test the sensitivity of parameters, a cross-validation technique was utilized. As mentioned previously, we further experimented on a second patient image, and the quantitative evaluation is given in Fig. 8. Recall the above definition of "Frangi1/2" and "Our method1/2", the first dataset acted as a training set with the second dataset a testing set in Fig. 8, and conversely in Fig. 7. Obviously, the testing results of the proposed method resembles much their training counterparts in both experiments. The Frangi filter is very robust to parameters, nearly no difference exists between the Frangi1 and Frangi2 curves. At the same time, there is also hardly a gap between the two different measures with our method on PR_v, but a small one on PR_s, see Fig. 8. In general, our method is not sensitive to parameters' change within a certain range.

6. Discussion and conclusions

In this paper, we have presented a 3D vessel enhancing filter based on the tensor invariants and strain energy density theory. The main feature is that we directly generalized the Hessian-based vesselness filters to non-tubular shapes and realized the enhancement of anisotropic vascular structures like bifurcations. Although the basic idea is motivated by existing achievements in strain en-

ergy analysis and diffusion tensor imaging, our novelties concentrate on different aspects:

- A strain energy density function is defined to measure strength of second-order derivative structures, and the sensitivity to anisotropy can be adjusted by a Poisson ratio parameter.
- Based on the intensity continuity assumption, a mathematical description of Hessian eigenvalues for general vessel shapes is given.
- Two tensor invariants, i.e. the mode of anisotropy and fractional anisotropy index are combined to form a shape discriminating function, and has been applied to a vessel likelihood measure.
- We introduced the volume-change invariant from tensor decomposition as a description of brightness contrast, and the theoretical interpretation is derived.
- The concept of relative Hessian strength has been introduced previously by other authors. Our work is to discover its ability in suppressing first-order step-edges and preventing fine structures from smoothing out by larger Gaussian kernels during the scale-space integration.

The performance of our method is demonstrated on both synthetic images and non-contrast-enhanced pulmonary CT data. It is shown that the proposed filter is effective in enhancing non-cylindrical structures or deformations like junctions compared to the other three vessel filters, and improves the connectivity of vessels. This has been validated not only from the 3D visualizations, but also with the quantitative *precision–recall* curves. For example, in the clinical data experiments, our method gained a more than 17% higher AUC_s measure among the four filters. Actually, the advantage is quite salient and useful, since the increased ratio came mainly from the challenging objects rather than the majority of normal vessels like large branches, which can be easily detected by most vessel extracting algorithms.

The improvement of connectivity will directly benefit the segmentation of vessel networks. In clinical imaging, the pulmonary vessel trees are widely used to infer or guess the boundaries of lung lobes, whose accuracy will depend on the completeness and reaching dept of neighboring vessel extraction. Moreover, the vascular bifurcations themselves are naturally intrinsic landmarks for image registration and navigation. Correspondingly, the enhancement of vessel junctions is desired in localization of progression and treatment of pulmonary diseases. In particular, the utilization of our filter is not limited to pulmonary images. Many vessel-related applications, such as the ridge tracking and curve evolution methods, rely on the vessel likelihood measure to define a driving speed function. The proposed strain energy filter will be a good choice, since it is able to preserve most desired vessels while suppressing unwanted noise and disturbance. Furthermore, even though the proposed filter did not directly generate an accurate vessel segmentation, the enhanced connection and presence can still be used as a topological prior to guide post-processing such as diameter quantification and aneurysm grading.

Presently, the proposed method is limited to 3D vessel images. It cannot be applied directly to 2D images because the orthogonal invariants, e.g. the mode of anisotropy may become invalid after adaption to 2D space. Further effort is needed to expand this model to more general structures and images. Although we have demonstrated the ability of Poisson ratio v parameter in controlling anisotropy, it is better to adaptively optimize its value to local varying structures rather than use a global one for the whole image. Then, an appropriate adjusting mechanism will be desired. Currently, the proposed method only utilized the magnitude information of the Hessian tensor. Although our filtering result was verified to be a good measure of vessel likelihood especially around the deformed structures, directional information is needed for more rubust segmentation of complex images. In this paper, we emphasized on the axial connectivity. It is likewise important to accurately estimate the radial vessel size or profile in many cases. Our future work will therefore focus on improving the quality of vessel detection with the strain energy filters.

Acknowledgments

This research was funded by STW (Grant LPG.07998) of the Netherlands and by the National Natural Science Foundation of China (Nos. 60835004 and 60871096). This work also benefitted from the use of the Insight Segmentation and Registration Toolkit (ITK), an open source software developed as an initiative of the US National Library of Medicine and available at http://www.itk.org.

Appendix A. Representation of strain energy density function with orthogonal components

The strain energy density function is originally defined as $U=\frac{1}{2}\sum_{i=1}^{3}\sum_{j=1}^{3}\sigma_{ij}\eta_{ij}$, and the corresponding principal stretches form is

$$U=\frac{1}{2}\sum_{k=1}^{3}\lambda_k\eta_k, \tag{A.1}$$

where λ_k and η_k are separately eigenvalues of stress and strain tensors. From Eq. (16), we have

$$\begin{bmatrix}\eta_1\\ \eta_2\\ \eta_3\end{bmatrix}=\frac{1}{E}\begin{bmatrix}1 & -v & -v\\ -v & 1 & -v\\ -v & -v & 1\end{bmatrix}\begin{bmatrix}\lambda_1\\ \lambda_2\\ \lambda_3\end{bmatrix}. \tag{A.2}$$

Then, Eq. (A.1) is rewritten to

$$U=\frac{1}{2E}\left[\lambda_1^2+\lambda_2^2+\lambda_3^2-2v(\lambda_1\lambda_2+\lambda_1\lambda_3+\lambda_2\lambda_3)\right]. \tag{A.3}$$

Consider $\overline{H}:\overline{H}=\frac{1}{3}(\lambda_1+\lambda_2+\lambda_3)^2$ and $\widetilde{H}:\widetilde{H}=\frac{1}{3}[(\lambda_1-\lambda_2)^2+(\lambda_1-\lambda_3)^2+(\lambda_2-\lambda_3)^2]$, we can further formulate the strain energy density as

$$U=\frac{1-2v}{2E}(\overline{H}:\overline{H})+\frac{1+v}{2E}(\widetilde{H}:\widetilde{H}). \tag{A.4}$$

Appendix B. Eigen decomposition of the second-order Taylor expansion term

Assume $\vec{e}_i$ and λ_i are the eigenvectors and eigenvalues of Hessian matrix, it is clear from eigen decomposition that

$$H_\sigma(x_0)=E\Lambda E^t. \tag{B.1}$$

Here, $E=(\vec{e}_1\vec{e}_2\vec{e}_3)$, and $\Lambda=diag\{\lambda_1,\lambda_2,\lambda_3\}$. Let $\vec{r}=c_1\vec{e}_1+c_2\vec{e}_2+c_3\vec{e}_3$, then the second-order Taylor expansion term can be written as

$$\begin{aligned}\vec{r}^tH_\sigma(x_0)\vec{r}&=\left(\sum_{i=1}^{3}c_i\vec{e}_i^t\right)E\Lambda E^t\left(\sum_{i=1}^{3}c_i\vec{e}_i\right)=\left(\sum_{i=1}^{3}c_i\vec{e}_i^tE\right)\Lambda\left(\sum_{i=1}^{3}c_iE^t\vec{e}_i\right)\\&=\begin{bmatrix}c_1 & c_2 & c_3\end{bmatrix}\Lambda\begin{bmatrix}c_1\\ c_2\\ c_3\end{bmatrix}=c_1^2\lambda_1+c_2^2\lambda_2+c_3^2\lambda_3.\end{aligned} \tag{B.2}$$

Thus, the second-order intensity continuity constraint of Eq. (22) is equivalent to $c_1^2\lambda_1+c_2^2\lambda_2+c_3^2\lambda_3=0$.

References

Adams, H., Bernard, M.S., McConnochie, K., 1991. An appraisal of ct pulmonary density mapping in normal subjects. Clinical Radiology 43 (4), 238–242.

Agam, G., Armato, S.G.I., Wu, C., 2005. Vessel tree reconstruction in thoracic ct scans with application to nodule detection. IEEE Transactions on Medical Imaging 24 (4), 486–499.

Antiga, L., 2007. Generalizing vesselness with respect to dimensionality and shape. The Insight Journal.

Bassera, P.J., Pierpaoli, C., 1996. Microstructural and physiological features of tissues elucidated by quantitative-diffusion-tensor mri. Journal of Magnetic Resonance, Series B 111 (3), 209–219.

Bauer, C., Pock, T., Sorantin, E., Bischof, H., Beichel, R., 2010. Segmentation of interwoven 3d tubular tree structures utilizing shape priors. Medical Image Analysis 14 (2), 172–184.

Bennink, H.E., van Assen, H.C., Streekstra, G.J., ter Wee, R., Spaan, J.A.E., ter Haar Romeny, B.M., 2007. A novel 3d multi-scale lineness filter for vessel detection. In: MICCAI 2007. Vol. 4792 of Lecture Notes in Computer Science. Brisbane, Australia, pp. 436–443.

Bitter, I., Uitert, R.V., Wolf, I., Ibanez, L., Kuhnigk, J.M., 2007. Comparison of four freely available frameworks for image processing and visualization that use itk. IEEE Transaction on Visualization and Computer Graphics 13 (3), 483–493.

Bower, A.F., 2009. Applied Mechanics of Solids. CRC Press, London.

Criscione, J.C., Humphrey, J.D., Douglas, A.S., Hunter, W.C., 2000. An invariant basis for natural strain which yields orthogonal stress response terms in isotropic hyperelasticity. Journal of the Mechanics and Physics of Solids 48 (12), 2445–2465.

Davis, J., Goadrich, M., 2006. The relationship between precision–recall and roc curves. In: Proceedings of the 23rd International Conference on Machine Learning. Vol. 148 of ACM International Conference Proceeding Series. Pittsburgh, Pennsylvania, pp. 233–240.

Descoteaux, M., Collins, D.L., Siddiqi, K., 2008. A geometric flow for segmenting vasculature in proton-density weighted mri. Medical Image Analysis 12 (4), 497–513.

Ennis, D.B., Kindlmann, G., 2006. Orthogonal tensor invariants and the analysis of diffusion tensor magnetic resonance images. Magnetic Resonance in Medicine 55 (1), 136–146.

Enquobahrie, A., Ibanez, L., Bullit, E., Aylward, S., 2007. Vessel enhancing diffusion filter. The Insight Journal.

Frangi, A.F., Niessen, W.J., Vincken, K.L., Viergever, M.A., 1998. Multiscale vessel enhancement filtering. In: Medical Image Computing and Computer-Assisted Interventation – MICCAI98. Lecture Notes in Computer Science, vol. 1496. Springer-Verlag, Berlin, Germany, pp. 130–137.

Gooya, A., Liao, H., Matsumiya, K., Masamune, K., Masutani, Y., Dohi, T., 2008. A variational method for geometric regularization of vascular segmentation in medical images. IEEE Transactions on Image Processing 17 (8), 1295–1312.

Haralick, R.M., Watson, L.T., Laffey, T.J., 1983. The topographic primal sketch. The International Journal of Robotics Research 2 (1), 50–72.

Hoffman, E.A., Reinhardt, J.M., Sonka, M., Simon, B.A., Guo, J., Saba, O., Chon, D., Samrah, S., Shikata, H., Tschirren, J., Beck, K.P.K.C., McLennan, G., 2003. Characterization of the interstitial lung diseases via density-based and texture-based analysis of computed tomography images of lung structure and function. Academic Radiology 10 (10), 1104–1118.

Hoffman, E.A., Simon, B.A., Mclennan, G., 2006. A structural and functional assessment of the lung via multidetector-row computed tomography: phenotyping chronic obstructive pulmonary disease. Proceedings of the American Thoracic Society 3 (6), 519–534.

Ibáñez, L., Schroeder, W., Ng, L., Cates, J., 2005. The ITK Software Guide, 2nd ed. Kitware, Inc. ISBN 1-930934-15-7.

Koller, T.M., Gerig, G., Szekely, G., Dettwiler, D., 1995. Multiscale detection of curvilinear structures in 2-d and 3-d image data. In: ICCV. Vol. ICCV'95 of Fifth International Conference on Computer Vision, p. 864.

Krissian, K., Malandain, G., Ayache, N., Vaillant, R., Trousset, Y., 2000. Model-based detection of tubular structures in 3d images. Computer Vision and Image Understanding 80 (2), 130–171.

Kuhnigk, J.M., Hahn, H., Hindennach, M., Dicken, V., Krass, S., Peitgen, H.O., 2003. Lung lobe segmentation by anatomy-guided 3d watershed transform. In: Medical Imaging 2003: Image Processing. Vol. 5032 of Proceedings of the SPIE. San Diego, CA, USA, pp. 1482–1490.

Li, Q., Sone, S., Doi, K., 2003. Selective enhancement filters for nodules, vessels, and airway walls in two- and three-dimensional ct scans. Medical Physics 30 (8), 2040–2051.

Lindeberg, T., 1998. Edge detection and ridge detection with automatic scale selection. International Journal of Computer Vision 30 (2), 117–154.

Lorenz, C., Carlsen, I.C., Buzug, T.M., Fassnacht, C., Weese, J., 1997. A multi-scale line filter with automatic scale selection based on the Hessian matrix for medical image segmentation. In: Scale-Space Theory in Computer Vision. Lecture Notes in Computer Science, vol. 1252/1997. Springer, Berlin, pp. 152–163.

Mahadevan, V., Narasimha-Iyer, H., Roysam, B., Tanenbaum, H.L., 2004. Robust model-based vasculature detection in noisy biomedical images. IEEE Transactions on Information Technology in Biomedicine 8 (3), 360–376.

Manniesing, R., Viergever, M.A., Niessen, W.J., 2006. Vessel enhancing diffusion: a scale space representation of vessel structures. Medical Image Analysis 10 (6), 815–825.

Manniesing, R., Viergever, M.A., Niessen, W.J., 2007. Vessel axis tracking using topology constrained surface evolution. IEEE Transactions on Medical Imaging 26 (3), 309–316.

Nain, D., Yezzi, A.J., Turk, G., 2004. Vessel segmentation using a shape driven flow. MICCAI 2004, vol. 1. Saint-Malo, France, pp. 51–59.

Qian, X., Brennan, M.P., Dione, D.P., Dobrucki, W.L., Jackowski, M.P., Breuer, C.K., Sinusas, A.J., Papademetris, X., 2009. A non-parametric vessel detection method for complex vascular structures. Medical Image Analysis 13 (1), 49–61.

Sato, Y., Nakajima, S., Atsumi, H., Koller, T., Gerig, G., Yoshida, S., Kikinis, R., 1997. 3d multi-scale line filter for segmentation and visualization of curvilinear structures in medical images. In: CVRMed/MRCAS'97. Vol. 1 of Proceedings of the 1st Joint Conference on CVRMed and MRCAS, pp. 213–222.

Sato, Y., Nakajima, S., Shiraga, N., Atsumi, H., Yoshida, S., Koller, T., Gerig, G., Kikinis, R., 1998. Three-dimensional multi-scale line filter for segmentation and visualization of curvilinear structures in medical images. Medical Image Analysis 2 (2), 143–168.

Sato, Y., Westin, C.F., Bhalerao, A., Nakajima, S., Shiraga, N., Tamura, S., Kikinis, R., 2000. Tissue classification based on 3d local intensity structure for volume rendering. IEEE Transactions on Visualization and Computer Graphics 6 (2), 160–180.

Sluimer, I., Schilham, A., Prokop, M., van Ginneken, B., 2006. Computer analysis of computed tomography scans of the lung. IEEE Transactions on Medical Imaging 25 (4), 385–405.

Sofka, M., Stewart, C.V., 2006. Retinal vessel centerline extraction using multiscale matched filters, confidence and edge measures. IEEE Transactions on Medical Imaging 25 (12), 1531–1546.

Stoel, B.C., Stolk, J.M., 2004. Optimization and standardization of lung densitometry in the assessment of pulmonary emphysema. Investigative Radiology 39 (11), 681–688.

ter Haar Romeny, B.M., 2003. Front-End Vision and Multi-scale Image Analysis. Kluwer Academic Publishers., Dordrecht.

Truc, P.T.H., Khan, M.A.U., Lee, Y.K., Lee, S., Kim, T.S., 2009. Vessel enhancement filter using directional filter bank. Computer Vision and Image Understanding 113 (1), 101–112.

Ukil, S., Reinhardt, J.M., 2009. Anatomy-guided lung lobe segmentation in X-ray ct images. IEEE Transactions on Medical Imaging 28 (2), 202–214.

van Bemmel, C.M., Viergever, M.A., Niessen, W.J., 2004. Semiautomatic segmentation and stenosis quantification of 3d contrast-enhanced mr angiograms of the internal carotid artery. Magnetic Resonance in Medicine 51 (4), 753–760.

Vasilevskiy, A., Siddiqi, K., 2002. Flux maximizing geometric flows. IEEE Transactions on Pattern Analysis and Machine Intelligence 24 (12), 1565–1578.

Verschakelen, J.A., Wever, W.D., 2007. Basic Anatomy and CT of the Normal Lung. Springer, Berlin, Heidelberg.

Weickert, J., 1997. A review of nonlinear diffusion filtering. In: Scale-Space Theory in Computer Vision. Lecture Notes in Computer Science, vol. 1252. Utrecht, The Netherlands, pp. 3–28.

Yushkevich, P.A., Piven, J., Hazlett, H.C., Smith, R.G., Ho, S., Gee, J.C., Gerig, G., 2006. User-guided 3d active contour segmentation of anatomical structures: significantly improved efficiency and reliability. Neuroimage 31 (3), 1116–1128.